Science Advances
www.advances.sciencemag.org/cgi/content/full/1/1/e1400035/DC1

# Supplementary Materials for

## Gelatin-derived sustainable carbon-based functional materials for energy conversion and storage with controllability of structure and component

Zhong-Li Wang, Dan Xu, Hai-Xia Zhong,Jun Wang, Fan-Lu Meng, Xin-Bo Zhang*

*Corresponding author. E-mail: xbzhang@ciac.ac.cn

Published 27 February 2015, *Sci. Adv.* **1**, e1400035 (2015)
DOI: 10.1126/sciadv.1400035

**This PDF file includes:**

Fig. S11. LSV curves of IAG-C before and after adding KCN in $O_2$-saturated 0.1 M KOH at 1600 rpm: (A) 10 mM KCN and (B) 50 mM KCN. The green line is the LSV curve after $CN^-$ poisoning tests, electrode washing, and immersion in fresh 0.1 M KOH for IAG-C.

Fig. S12. LSV curves at different rotation rates in $O_2$-saturated 0.1 M KOH at 5 mV $s^{-1}$, and the inset shows the corresponding K-L plots: (A) G-C, (B) AG-C, (C) IG-C, and (D) Pt/C; (E) electron transfer number (n) and (F) peroxide yield of G-C, AG-C, IG-C, IAG-C, and commercial 20 wt % Pt/C in $O_2$-saturated 0.1 M KOH.

Fig. S13. (A) Linear sweep voltammetry (LSV) curves for G-C, AG-C, IG-C, IAG-C, and Pt/C in $O_2$-saturated 0.1 M $HClO_4$ at 5 mV $s^{-1}$ at 1600 rpm; LSV curves for IAG-C (B) and Pt/C (C) at different rotation rates in $O_2$-saturated 0.1 M $HClO_4$ at 5 mV $s^{-1}$, and the inset shows the K-L plots.

Fig. S14. (A) Electron transfer number and (B) peroxide yield (n) of G-C, AG-C, IG-C, IAG-C, and commercial 20 wt % Pt/C in $O_2$-saturated 0.1 M $HClO_4$; (C) chronoamperometric response of IAG-C and Pt/C in $O_2$-saturated 0.1 M $HClO_4$ followed by addition of 3 M methanol; (D) chronoamperometric response of IAG-C and Pt/C in $O_2$-saturated 0.1M $HClO_4$ solution at 0.5 V (versus RHE) at 1600 rpm.

Fig. S15. (A) High-angle annular dark-field scanning transmission electron microscopy (STEM) image of the IAG-C catalyst; (B) C-, (C) N-, (D) O-, and (E) Fe-elemental mapping of the square region.

Fig. S16. (A) High-angle annular dark-field scanning transmission electron microscopy (STEM) image of the IAG-C catalyst; (B) C-, (C) N-, (D) O-, and (E) Fe-elemental mapping of the square region after stability test. (F) N 1s XPS spectra of IAG-C after stability test.

Fig. S17. TEM images of $Fe_3O_4$@AGC with different content of $Fe_3O_4$ in the hybrids: (A) $Fe_3O_4$@AGC-4, (B) $Fe_3O_4$@AGC, and (C) $Fe_3O_4$@AGC-6; (D) TG curves of the three hybrids to determine the content of carbon; (E) XRD patterns of three hybrids. The diffraction peaks of the composites are perfectly indexed to pure-phase $Fe_3O_4$ (JCPDS No.65-3107).

Fig. S18 Charge-discharge curves of $Fe_3O_4$@AGC (A), bare $Fe_3O_4$ (B), and AGC (C) at a current density of 100 mA $g^{-1}$; (D) Nyquist plots for the $Fe_3O_4$@AGC and bare $Fe_3O_4$-based cells with lithium metal as counter electrode.

Fig. S19. The calibration CV curves of Ag/AgCl electrode (A) in 0.1 M KOH and (B) in 0.1 M $HClO_4$ with respect to RHE.

# Supplementary Materials

## Materials and Methods

### 1. Chemicals and Materials

Gelatin (Aladdin, CP), Iron nitrate (Aladdin, AR), Ammonium nitrate (Tianjin Huadong Reagent, AR), Hydrochloric acid (HCl, 36%-38%, Beijing Chemical Work, AR), Polyvinylidenefluoride (PVDF, DuPont Company, 99.9%), N-methyl-2-pyrrolidinone (NMP, Aladdin Reagent, AR), Electrolyte (1 mol $L^{-1}$ $LiPF_6$ in a mixture of ethylene carbonate (EC) and dimethyl carbonate (DMC) (1:1, by volume)) Zhangjiagang Guotai-Huarong New Chemical Materials Co., Ltd).

### 2. Materials characterization

The morphology is observed with scanning electron microscopy (SEM, HITACHI S-4800) opreated at 10 kV and transmission electron microscopy (TEM, FEI Tacnai G2) with an accelerating voltage of 200 kV. X-ray photoelectron spectroscopy (XPS) measurements are performed on an ESCALAB 250 photoelectron spectrometer. Raman spectra are measured and collected using a 532 nm laser by a RENISHAW. The specific surface areas are determined by a Micrometritics ASAP 2020 analyzer. Thermogravimetric analysis (TG) was carried out using a Mettler Toledo TGA-SDTA851 analyzer (Switzerland) from 25 to 800 $^{o}$C in a air flow at a heating rate of 10 $^{o}$C/min. Wide-angle X-ray diffraction (XRD) patterns were collected on Bruker D8 Focus Powder X-ray diffractometer using Cu Kαradiation (40 kV, 40 mA). Mössbauer spectra are recorded at room temperature in the transmission mode using MS 500 (Oxford Instruments, U.K.) with a 25 mCi $^{57}$Co/Pd-source, and the calibration is made with respect to α-Fe.

**Table S1** Summary of chemical compositions analyzed by XPS and ICP-OES and texture parameters obtained from nitrogen adsorption analysis

| Sample | Composition (at%, by XPS) | | | | Pore volume (cm$^{-3}$ g$^{-1}$) | Surface area (m$^2$ g$^{-1)}$ |
|---|---|---|---|---|---|---|
| | C | O | N | Fe | | |
| G-C | 90.62 | 5.06 | 4.32 | - | 0.101 | 189.8 |
| AG-C | 90.85 | 4.90 | 4.25 | - | 0.419 | 725.3 |
| IG-C | 93.05 | 3.19 | 3.64 | 0.12 | 0.385 | 598.8 |
| IAG-C | 93.53 | 2.67 | 3.66 | 0.14 | 1.025 | 1215.4 |

**Table S2** Comparison of onset and half-wave potentials (*vs.* RHE) from LSV curves between this work and other independent literatures. All are in alkaline condition with 0.1 M KOH.

| References | Materials | Loading (mg cm$^{-2}$) | Onset potential (V) | half-wave potential (V) |
|---|---|---|---|---|
| This work | Gelatin-derived porous Fe-N-C | 0.3 | 1.02 | 0.87 |
| Nat. Commun. 2013, 4, 1922 | N-Fe-co-doped carbon black | 0.2 | | 0.87 |
| Adv. Mater. 2014, 26, 1450 -1455 | Co-N-C from cobalt porphyrin conjugated polymer | 0.6 | 0.83 | 0.77 |
| Adv. Mater. 2013, 25, 998-1003 | Fe@$Fe_3C$-loaded N-doped carbon spheres | unknown | 0.85 | |
| Angew. Chem. Int. Ed. 2014, 53, 2433-2437 | Fe-N-C from covalent organic polymers | 0.2 | 0.98 | |
| Angew. Chem. Int. Ed. 2014, 53, 3675-3679 | $Fe_3C$/C hollow spheres | 0.6 | 1.05 | 0.83 |
| Angew. Chem. Int. Ed. 2011, 50, 11756-11760 | B-N-co-doped carbon nanotubes | unknown | | 0.73 |
| Angew. Chem. Int. Ed. 2014, 53, 4102-4106 | Heteroatom doped carbon nanotubes | unknown | 0.92 | 0.82 |
| J. Am. Chem. Soc. 2012, 134, 18932-18935 | Nitrogen-doped graphene quantum dots | unknown | 0.94 | |
| Nat. Mater. 2011, 10, 780 -786 | $Co_3O_4$/N-rmGO hybrid | 0.17 | 0.88 | 0.83 |
| Nat. Chem. 2011, 3, 79-84 | $Co_xMn_{3-x}O_4$ nanoparticles | unknown | 0.88 | |
| J. Am. Chem. Soc., 2012, 134, 9082-9085 | N-doped graphene aerogel-supported $Fe_3O_4$ | unknown | 0.76 | |
| Angew. Chem. Int. Ed. 2013, 52, 2474 -2477 | $MnO_2$ with Vacancies | 0.07 | $\approx$0.85 | |

**Table S3** Mössbauer parameters for the fitted lines and their assignments for various samples

| Samples | | $\delta_{iso}$ (mm $s^{-1}$) | $E_Q$ (mm $s^{-1}$) | Ho (KOe) | FWHM (mm $s^{-1}$) | Area ratio (%) | Assignment |
|---|---|---|---|---|---|---|---|
| IG-C | Sing | -0.02±0.01 | – | – | 0.12±0.01 | 1.2 | Superparamagnetic iron[1,2] |
| | D1 | 0.36±0 | 1.18±0 | – | 0.36±0 | 38.1 | $Fe^{II}N_4$/C, low spin[3-5] |
| | D2 | 0.21±0.02 | 2.33±0.03 | – | 0.82±0 | 24.9 | $Fe^{II}N_{2+2}$/C, intermediate spin[6,7] |
| | D3 | 0.80±0.01 | 2.28±0.02 | – | 0.46±0.01 | 17.7 | N–$Fe^{II}N_{2+2}$/C, high spin[8] |
| | Sext 1 | -0.02±0 | -0.04±0.02 | 328.8±0.6 | 0.12±0 | 4.8 | α-Fe[1,2] |
| | Sext 2 | 0.22±0 | -0.02±0.01 | 209.1±0.5 | 0.21±0 | 13.3 | Iron carbide[1,2] |
| IAG-C | Sing | -0.02±0.01 | – | – | 0.15±0.02 | 5.0 | Superparamagnetic iron[1,2] |
| | D1 | 0.31±0.01 | 0.98±0.01 | – | 0.44±0 | 62.0 | $Fe^{II}N_4$/C, low spin[3-5] |
| | D2 | 0.15±0.05 | 2.54±0.1 | – | 0.53±0.04 | 14.5 | $Fe^{II}N_{2+2}$/C, intermediate spin[6,7] |
| | D3 | 0.93±0.03 | 2.03±0.07 | – | 0.21±0.03 | 5.6 | N–$Fe^{II}N_{2+2}$/C, high spin[8] |
| | Sext 1 | -0.10±0.04 | 0.09±0.08 | 322.2±3 | 0.15±0.02 | 8.6 | α-Fe[1,2] |
| | Sext 2 | 0.13±0.03 | 0.20±0.06 | 224.1±2 | 0.20±0.02 | 4.3 | Iron carbide[1,2] |

[1] N. N. Greenwood, T. C. Gibb, Mössbauer Spectroscopy; 1st ed.; Chapman and Hall Ltd.: London, 1971; Vol. 1.

[2] U. I. Kramm, M. Lefèvre, N. Larouche, D. Schmeisser, J. P. Dodelet, *J. Am. Chem. Soc.* **2014**, *136*, 978.

[3] U. I. Koslowski, I. Abs-Wurmbach, S. Fiechter, P. Bogdanoff, *J. Phys. Chem. C* **2008**, *112*, 15356.

[4] A. L. Bouwkamp-Wijnoltz, W. Visscher, J. A. R. v. Veen, E. Boellaard, A. M. v. d. Kraan, S. C. Tang, *J. Phys. Chem. B* **2002**, *106*, 12993.

[5] M. Ferrandon, A. J. Kropf, D. J. Myers, K. Artyushkova, U. Kramm, P. Bogdanoff, G. Wu, C. M. Johnston, P. Zelenay, *J. Phys. Chem. C* **2012**, *116*, 16001.

[6] C. A. Melendres, *J. Phys. Chem.* **1980**, *84*, 1936.

[7] R. Taube, *Pure Appl. Chem.* **1974**, *38*, 427.

[8] U. I. Kramm, J. Herranz, N. Larouche, T. M. Arruda, M. Lefévre,; F. Jaouen, P. Bogdanoff, S. Fiechter, I. Abs-Wurmbach, S. Mukerjee, J.-P. Dodelet, *Phys. Chem. Chem. Phys.* **2012**, *14*, 11673.

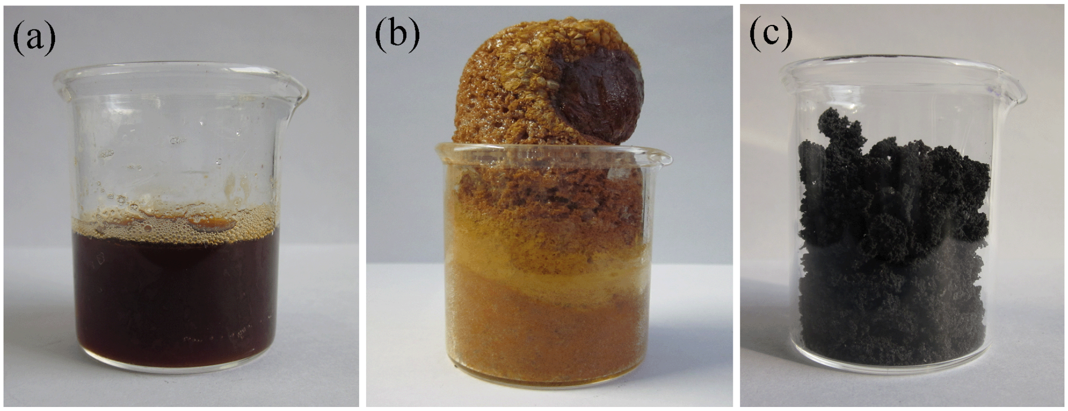

**Fig. S1.** Photographs of precursor solution (a), composite gel (b), and the final catalyst (c).

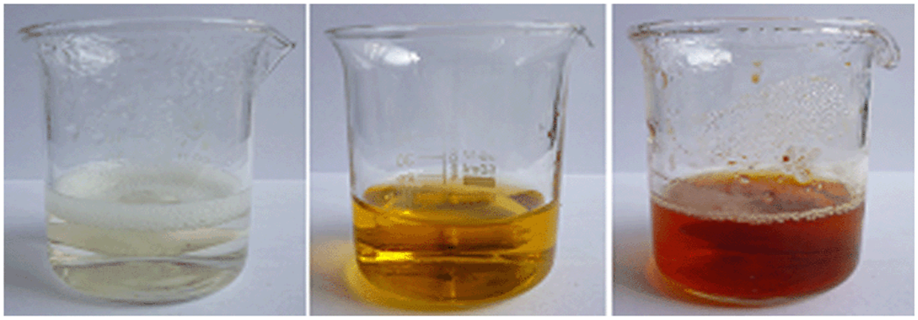

Gelatin solution Fe(NO$_3$)$_3$ solution Gelatin+Fe(NO$_3$)$_3$ solution

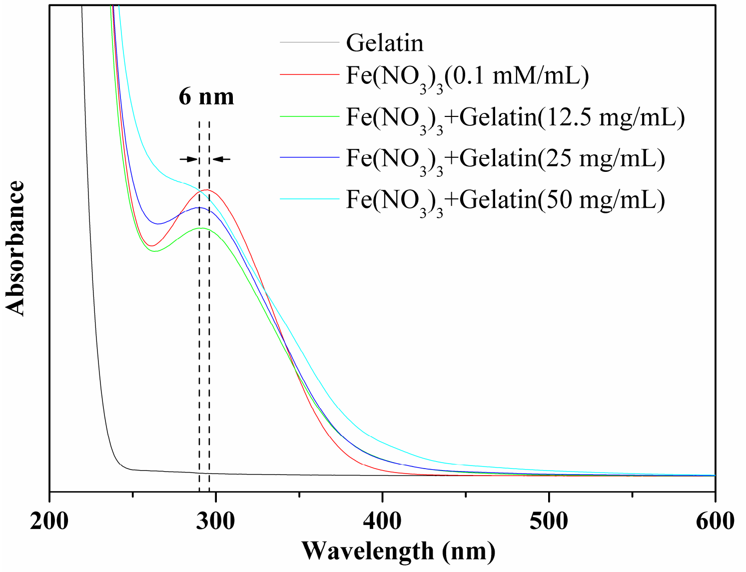

**Fig. S2.** Comparison of photographs and UV-Vis spectroscopy of different solutions.

UV-visible spectroscopy shows the absorbance peaks of iron ions exhibits an obvious blue-shift of 6 nm with the addition of gelatin, indicating strong binding of the precursor iron cation to functional groups of the gelatin, and the intensities of absorbance increase with increasing gelatin concentration.

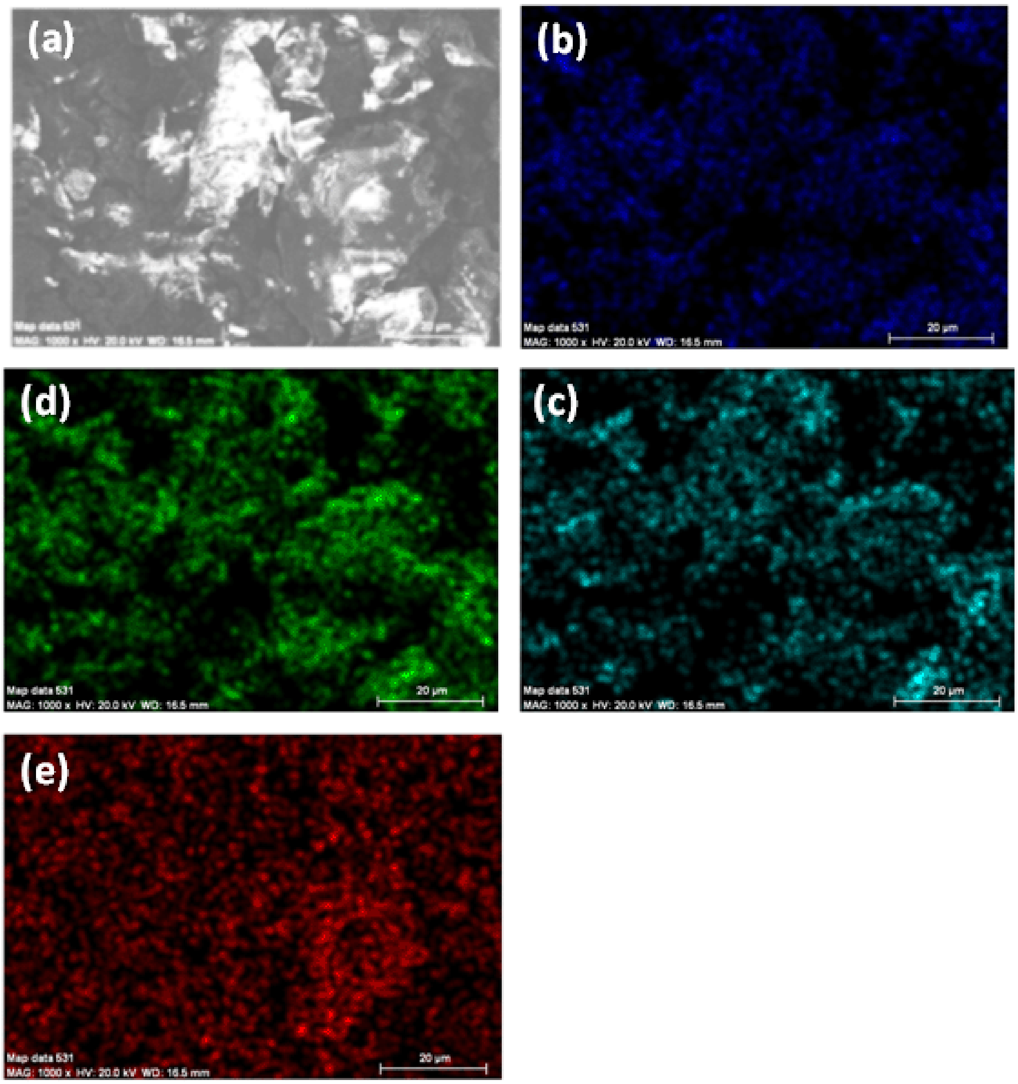

**Fig. S3.** (a) SEM image of composite gel after sol-gel; (b-e) Mapping analysis of the composite gel: (b) C element from gelatin, (c) N and (d) O elements from gelatin and ammonium nitrate, (e) Fe element from iron ferric hydroxide.

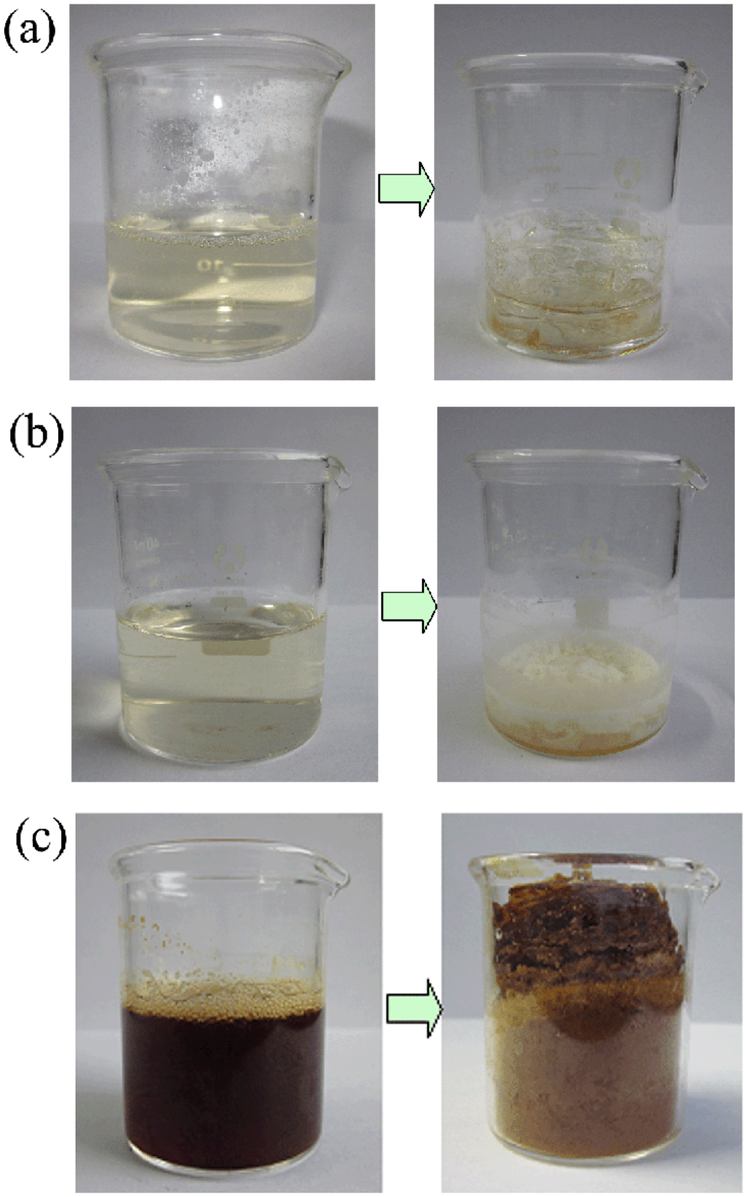

**Fig. S4.** Comparison of the products derived from different precursor solution containing different components at the same treatment conditions: (a) only gelatin; (b) gelatin and ammonium nitrate; and (c) gelatin and iron nitrate.

From the comparative experiments, it can be seen that the precursor solution containing only gelatin and ammonium nitrate form the transparent sheet-like solid solution without any sol-gel phenomenon. In contrary, for the solution containing gelatin and iron nitrate, a uniform brown gel is formed after thermal treatment with volume expansion. The addition of ammonium nitrate further increases the volume expansion of the composite gel compared to the absence of it.

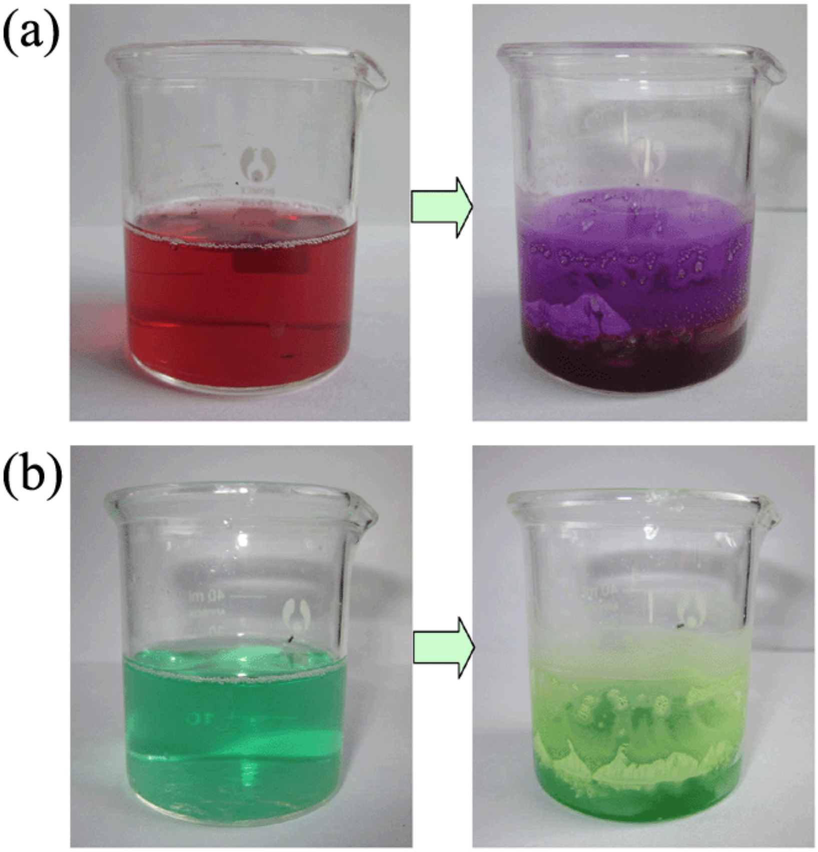

**Fig. S5.** Comparison of gels obtained by using cobalt nitrate (a) and nickel nitrate (b) as metal salts with the same treatment conditions of iron nitrate.

Another interesting phenomenon should be noted that the sol-gel chemistry of gelatin has certain selectivity toward metal ions. As shown in Fig. S4, cobalt nitrate and nickel nitrate can not form composite gels at the same conditions due to the coordinating selectivity of gelatin and the hydrolysis capabilities of metal ions.

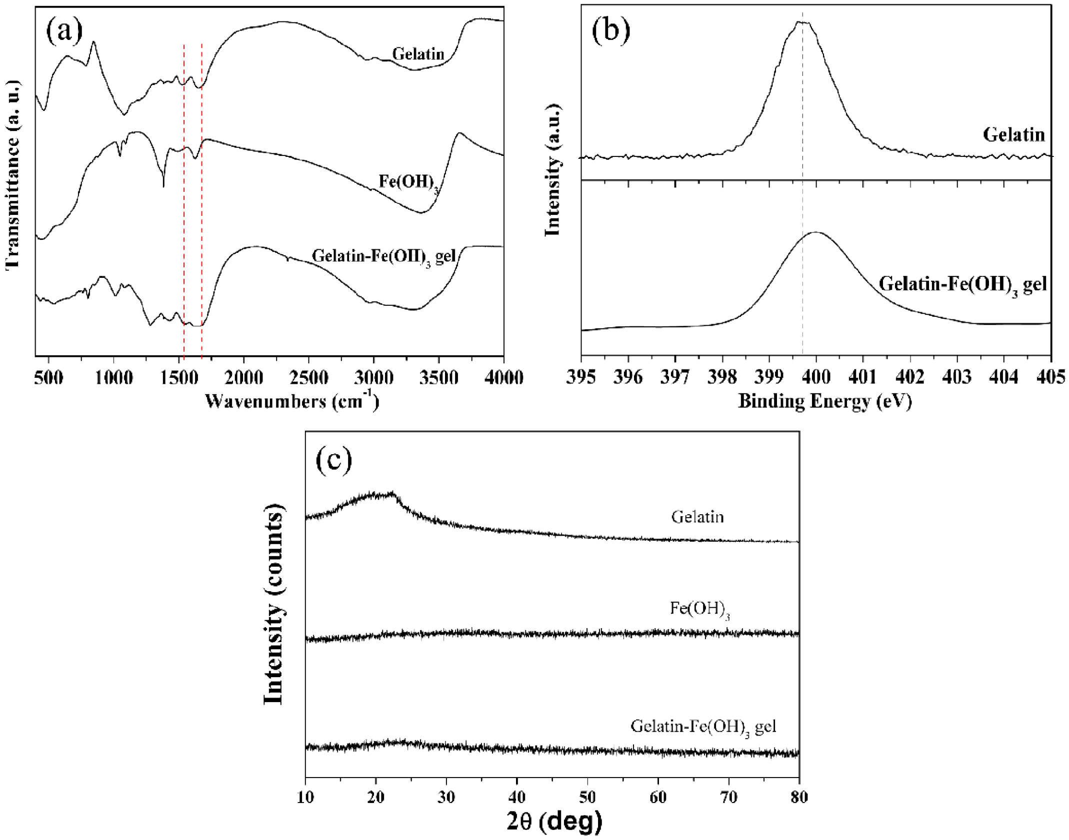

**Fig. S6.** (a) FT-IR spectra, (b) N 1s spectra and (c) XRD patterns of gelatin, amorphous $Fe(OH)_3$, and gelatin-$Fe(OH)_3$ gel.

The carboxyl and amide groups of composite gel both shift toward high wave-number compared to that of the pure gelatin (Fig. S6a). At the same time, a positive shift in N 1s spectra is observed, indicating that the coordination of long-pair electrons of N to Fe unoccupied molecular orbitals (Fig. S6b). From the XRD patterns, it can be also found that a broad diffraction peak for pure gelatin disappears after gelation with iron nitrate (Fig. S6c), further indicating the relative ordered chains of gelatin are dispersed in the composite gel under the interaction with metal ions.

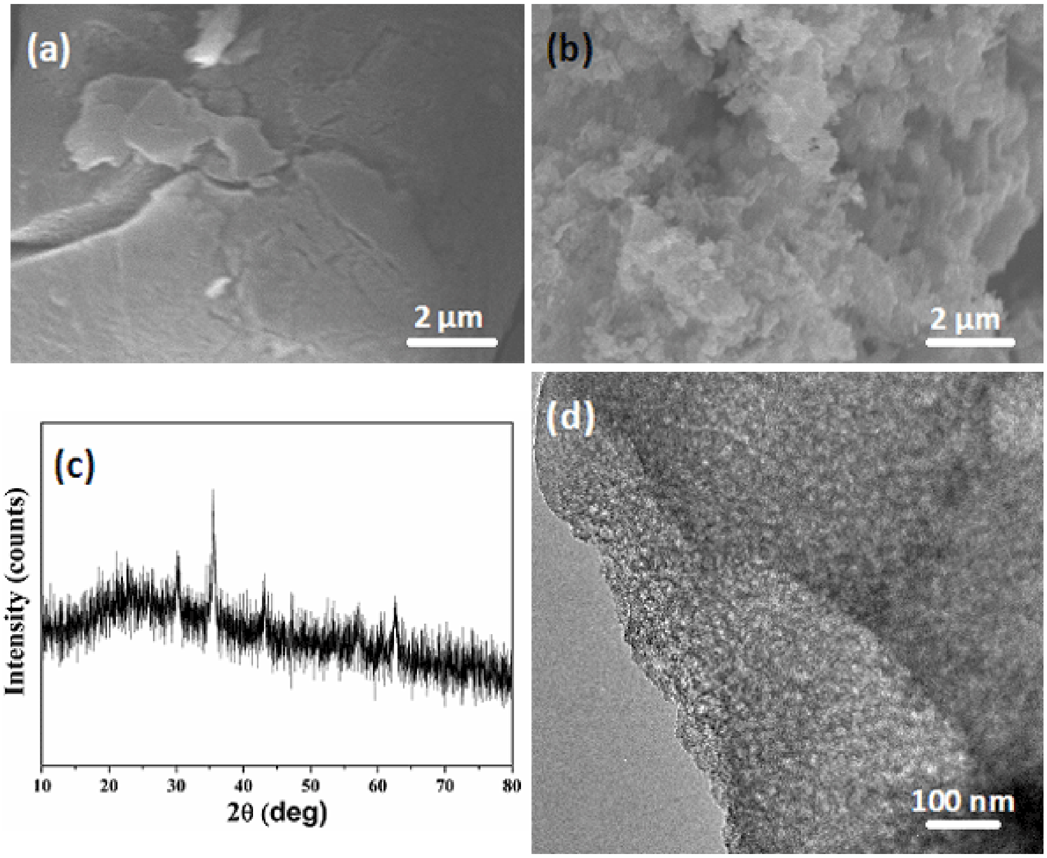

**Fig. S7.** (a) SEM image of composite gel after sol-gel; (b) SEM image and (c) XRD pattern of the product obtained by calcining the gel at 350 $^{o}$C; (d) TEM image of the above HCl-washed product.

From the SEM images, it can be clearly observed that the gel is big dense bulk before thermal decomposition, while after the treating in high temperature the product is loosely-packed small particles.

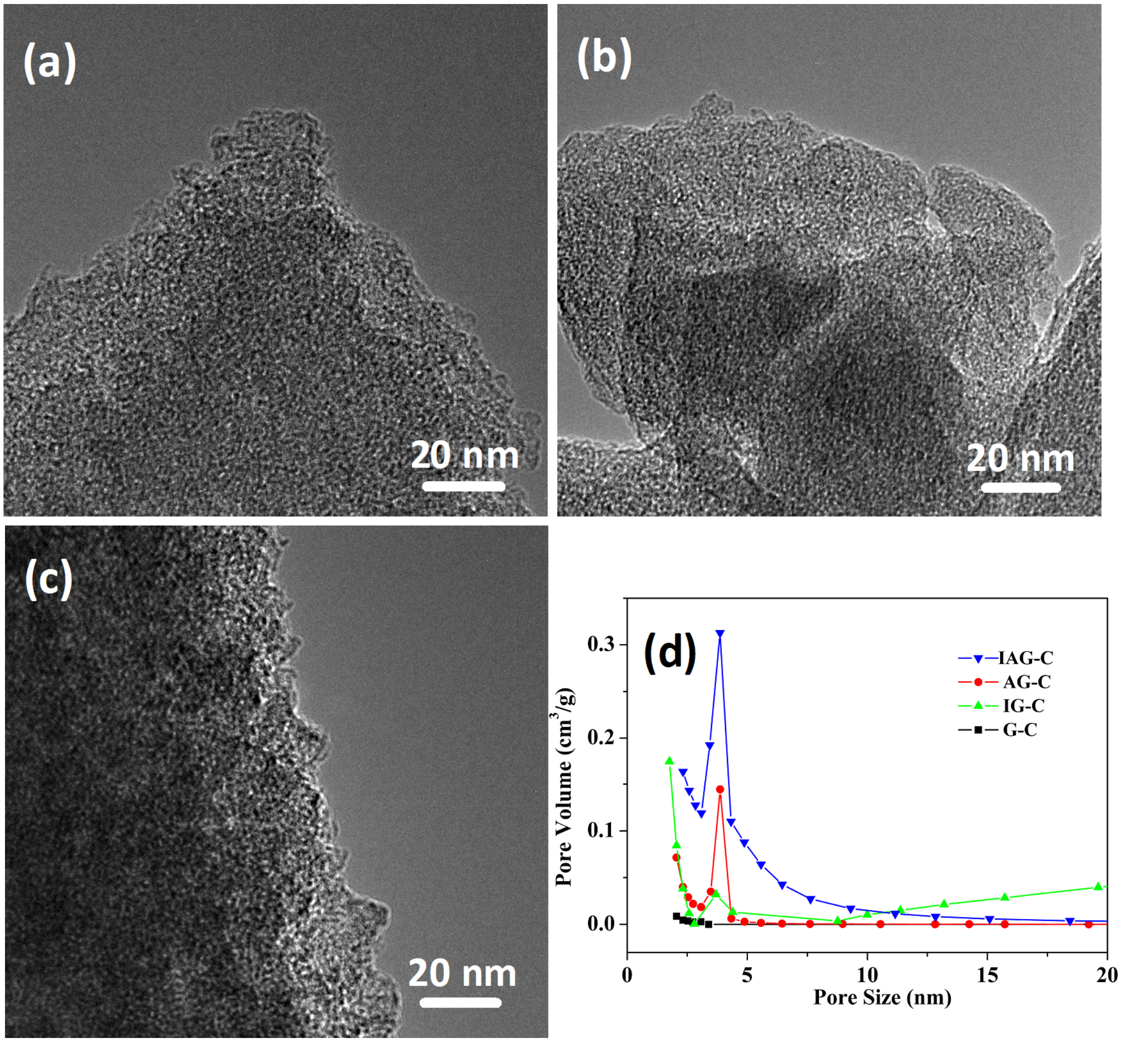

**Fig. S8.** TEM images of AG-C (a), IG-C (b), and G-C (c); (d) Pore size distributions of four samples prepared with different precursors.

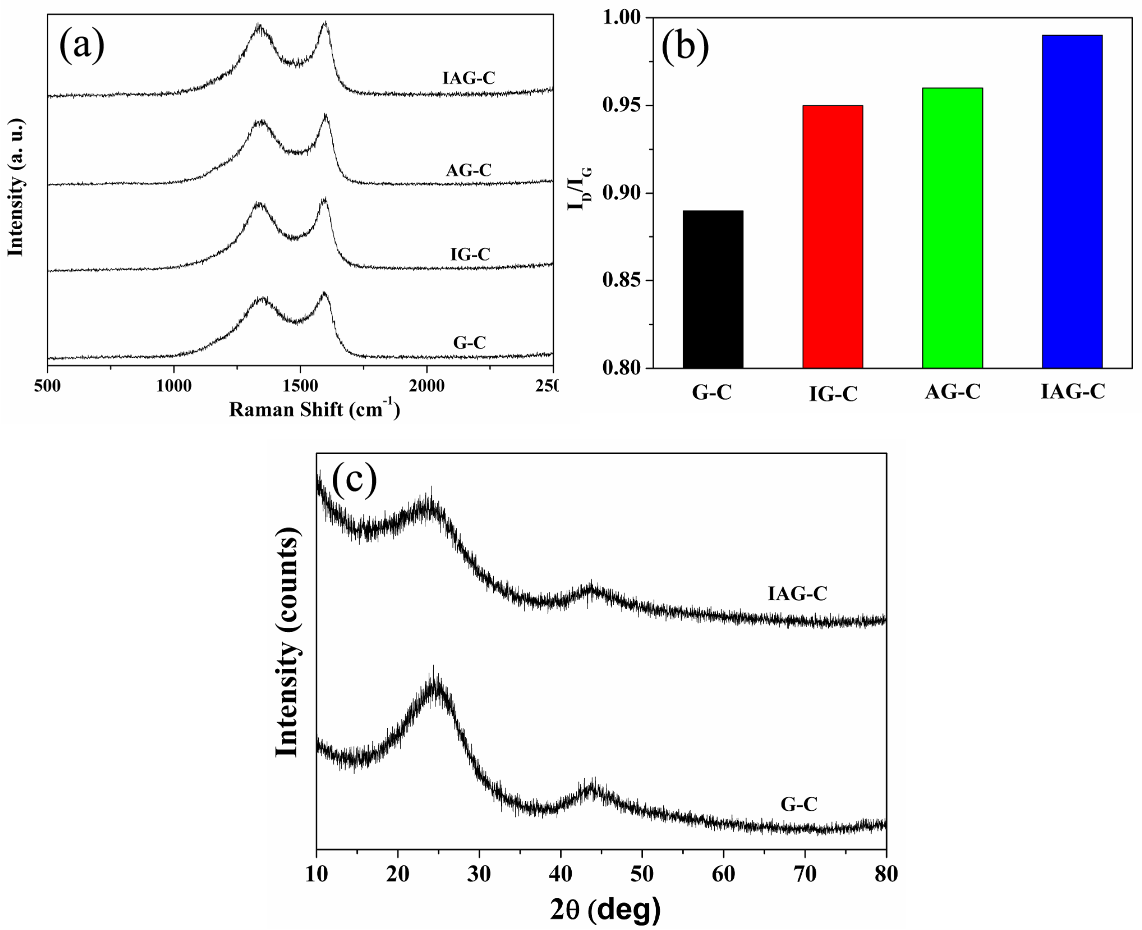

**Fig. S9.** Raman spectra (a), and $I_D/I_G$ ratio (b) of four samples prepared with different precursors. (c) Comparison of XRD patterns of IAG-C and G-C.

The changes of carbon microstructure can be further reflected by Raman spectra and XRD patterns (Fig. S9a). From sample G-C to IAG-C, the values of $I_D/I_G$ gradually increase from 0.89 to 099 (Fig. S9b) and the broad diffraction peaks of graphite become gradually weak (Fig. S9c), indicating the amorphous and defect carbon structure increases with the increase of the surface area.

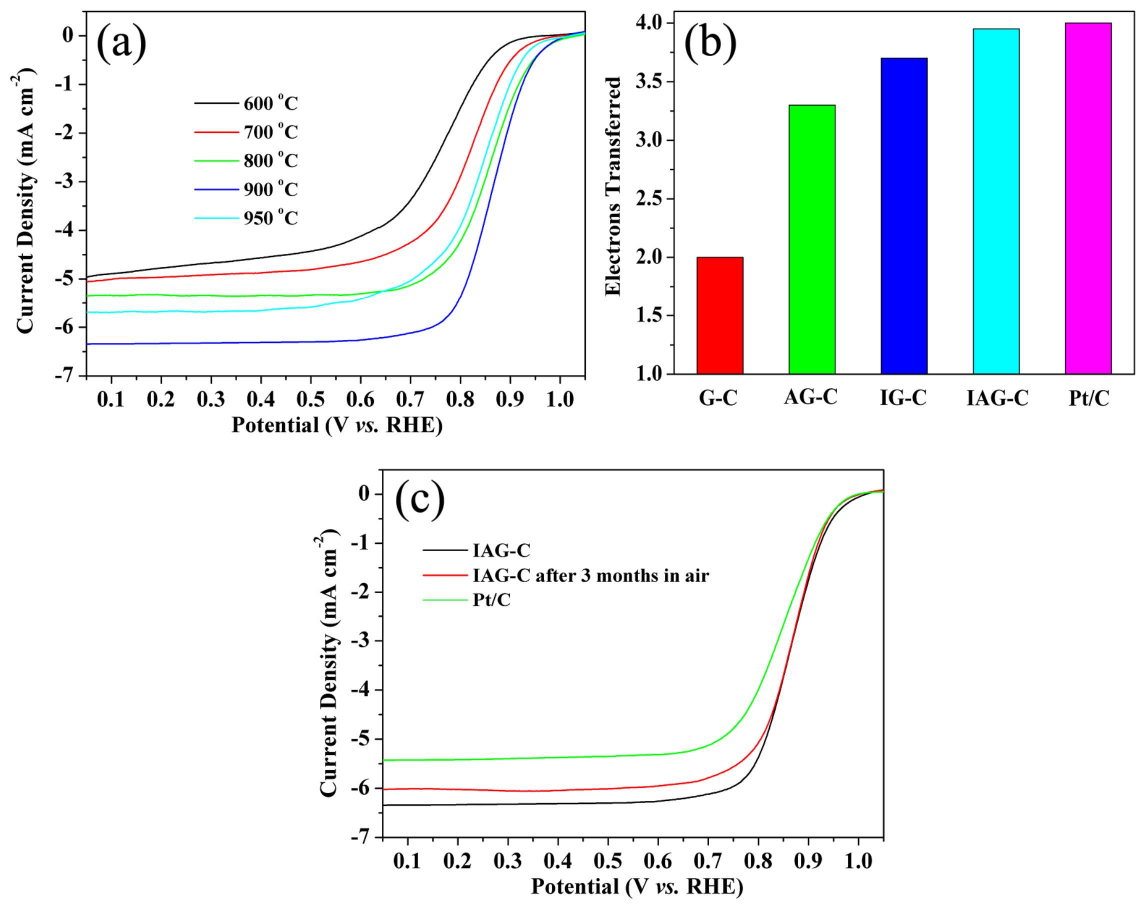

**Fig. S10.** (a) Temperature effect of IAG-C activity for ORR; (b) Comparison of the electron transfer number of catalysts at 0.65 V; (c) Stability of IAG-C after three months in air.

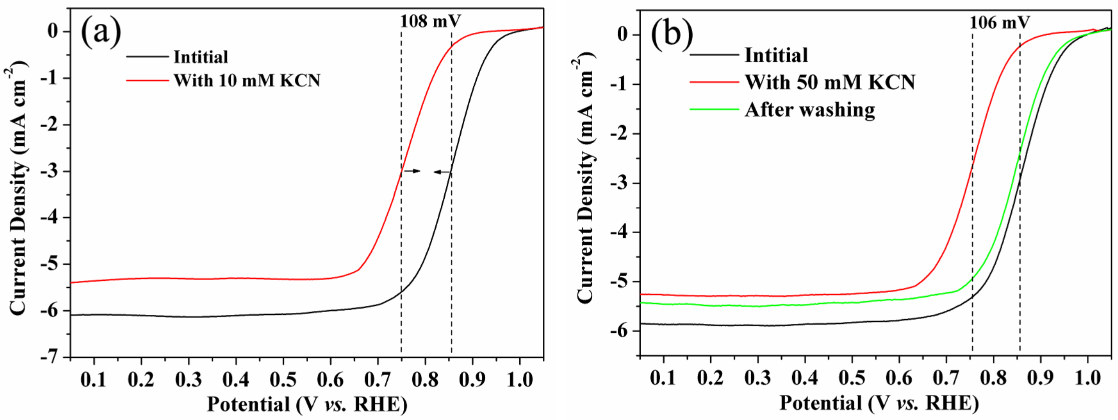

**Fig. S11.** LSV curves of IAG-C before and after adding KCN in $O_2$-saturated 0.1 M KOH at 1600 rpm: (a) 10 mM KCN and (b) 50 mM KCN. The green line is the LSV curve after $CN^-$ poisoning tests, electrode washing, and immersion in fresh 0.1 M KOH for IAG-C.

In order to assess the role of iron in forming active ORR catalytic sites on Fe-N-C catalysts, we investigated the ORR activity of IAG-C in 0.1 M KOH containing 10 mM and 50 mM KCN, respectively, ensuring enough $CN^-$ to interact with Fe ions. $CN^-$ ions are known to coordinate strongly to iron and poison the iron-centred catalytic sites for ORR. With the addition of $CN^-$, the ORR half-wave potential of the Fe-N-C catalyst decreases significantly by 106～108 mV with the decrease of diffusion-limiting current, suggesting blocking of the iron sites by $CN^-$ ions. The CN- ions bind with a high affinity to many oxidized Fe(III) complexes but possess a minimal affinity to reduced Fe(II) species. For the Fe(II)-$N_4$/C active sites, once the Fe(II)-$O_2$ complex is formed during ORR process, a single electron transfer from Fe(II) to $O_2$ occurs immediately, forming Fe(III)-$O_2^{\bullet -}$. Due to the high affinity of $CN^-$ ions to the Fe(III) metal center, the adsorbed superoxide molecule ($O_2^{\bullet -}$) will immediately be replaced by $CN^-$ ions, which makes the Fe-$N_4$ sites inactive for ORR. The release of the superoxide molecule will result in the formation of $HO_2^-$ species, leading to the inefficient two-electron reduction in an alkaline solution.[46] It is worth noting that the residual activity after $CN^-$ poisoning is still high due to the N-doped carbon active centers, which is inert to the poison of $CN^-$ ions. The incorporation of electron-accepting nitrogen atoms in the conjugated carbon plane produces a relatively high positive charge density on the adjacent carbon atoms, which induces the active sites for the ORR. These results demonstrate that both Fe-based (Fe-$N_x$/C) and N-based (N-C functional groups such as graphite-like or pyridine-like N groups) two types of active sites always co-exist in the Fe-N-C catalysts and simultaneously contribute the ORR catalytic activity.

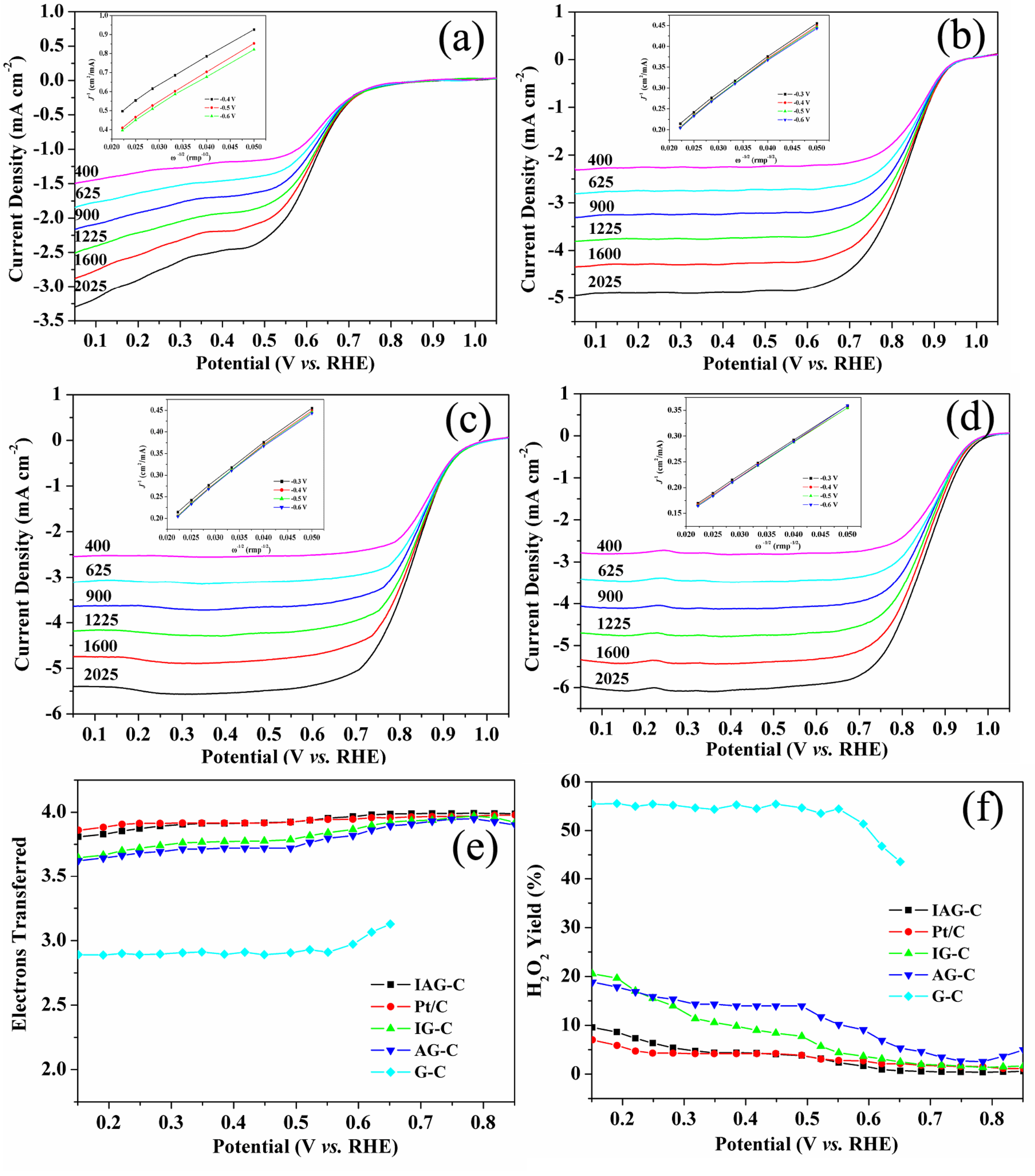

**Fig. S12.** LSV curves at different rotation rates in $O_2$ saturated 0.1 M KOH at 5 mV $s^{-1}$, and the inset shows the corresponding K-L plots: (a) G-C, (b) AG-C, (c) IG-C, and (d) Pt/C; (e) Electron transfer number (*n*) and (f) Peroxide yield of G-C, AG-C, IG-C, IAG-C, and commercial 20 wt% Pt/C in $O_2$-saturated 0.1 M KOH, respectively.

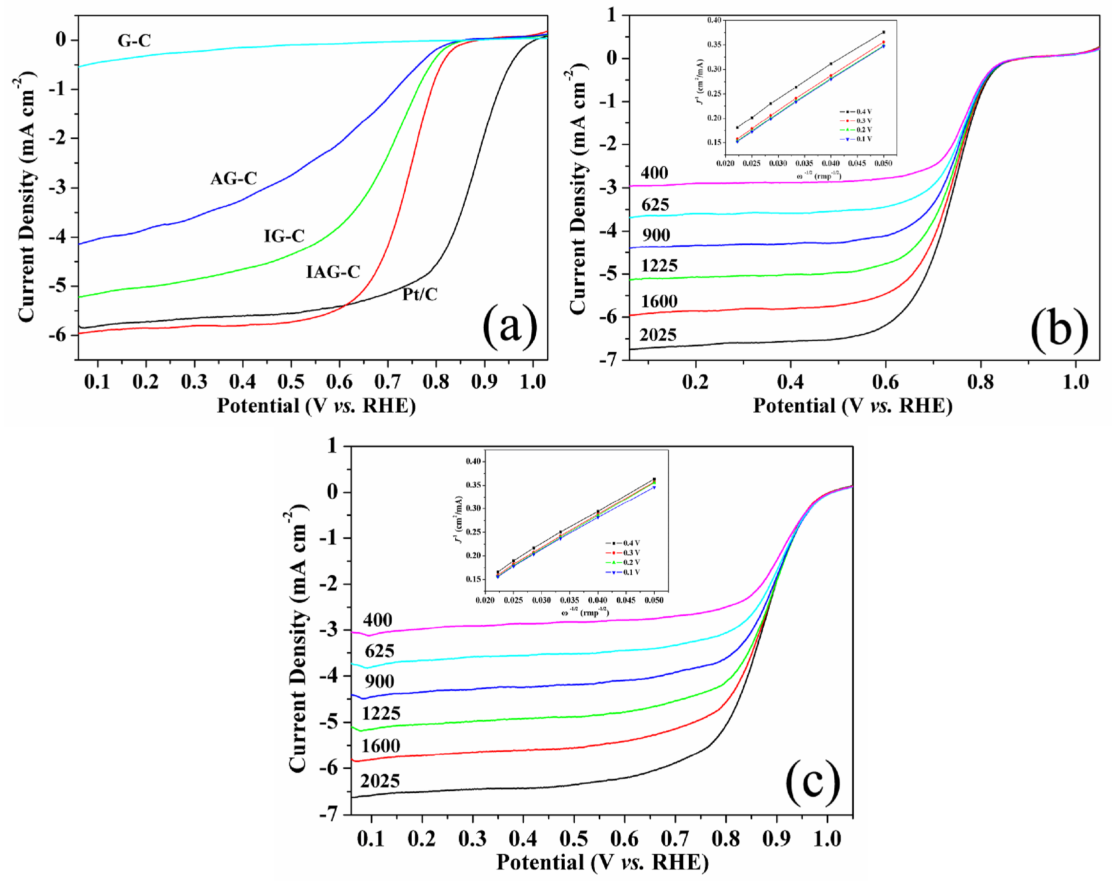

**Fig. S13.** (a) Linear sweep voltammetry (LSV) curves for G-C, AG-C, IG-C, IAG-C, and Pt/C in $O_2$ saturated 0.1 M $HClO_4$ at 5 mV $s^{-1}$ at 1600 rpm; LSV curves for IAG-C (b) and Pt/C (c) at different rotation rates in $O_2$ saturated 0.1 M $HClO_4$ at 5 mV $s^{-1}$, and the inset shows the K-L plots.

IAG-C catalyst is found to be an effective ORR catalyst in acidic media as well. The catalytic activity is much higher compared with that of IG-C, AG-C, G-C, and some carbon materials reported elsewhere. The transferred electron number (*n*) per $O_2$ molecule for the IAG-C electrode in the acidic medium calculated by the K-L equation is 3.9-4.0 at 0.1–0.4 V.

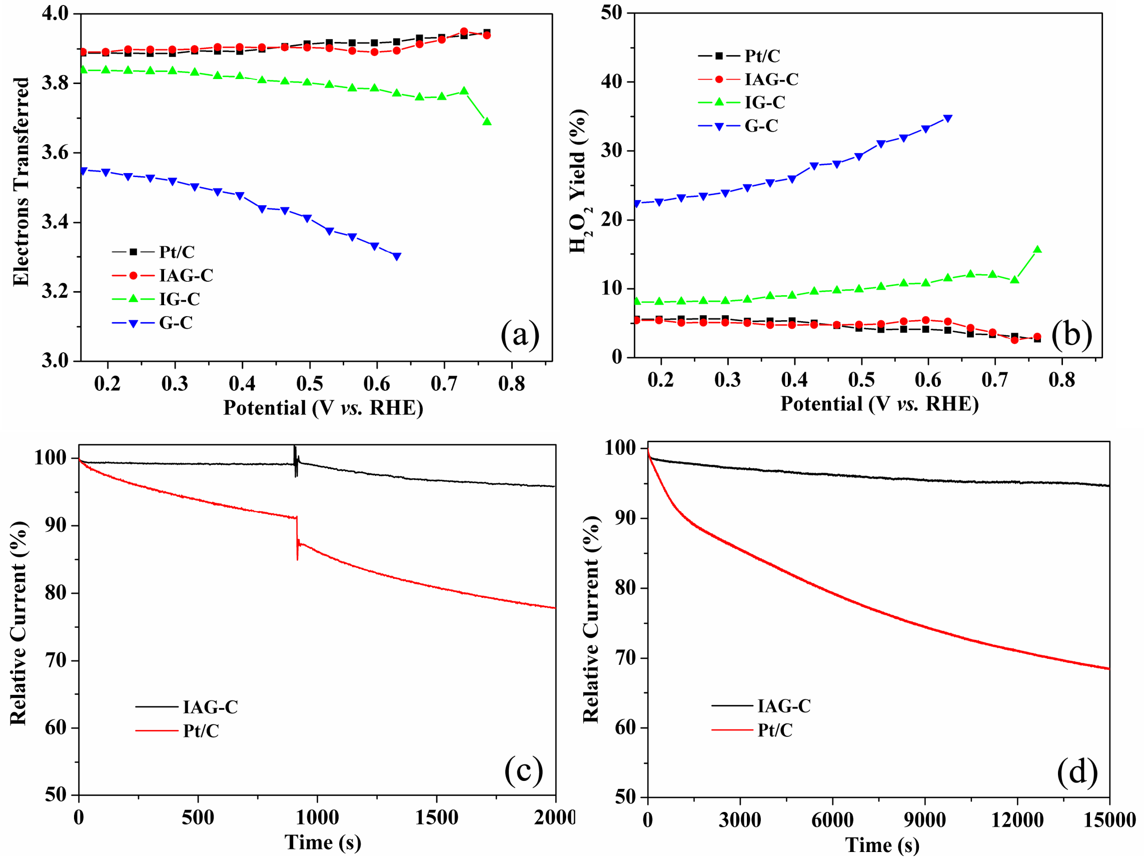

**Fig. S14.** (a) Electron transfer number and (b) Peroxide yield (*n*) of G-C, AG-C, IG-C, IAG-C, and commercial 20 wt% Pt/C in $O_2$-saturated 0.1 M $HClO_4$, respectively; (c) Chronoamperometric response of IAG-C and Pt/C in $O_2$ saturated 0.1 M $HClO_4$ followed by addition of 3 M methanol; (d) Chronoamperometric response of IAG-C and Pt/C in $O_2$ saturated 0.1M $HClO_4$ solution at 0.5 V (*vs.* RHE) at1600 rpm.

The calculated yield of $H_2O_2$ for the IAG-C electrode is less than 10% under the potential range of 0.15-0.75 V. The transferred electron number (*n*) per $O_2$ molecule for the IAG-C electrode in the acidic medium calculated is also 3.9-4.0 at 0.15–0.75 V by the RRDE curves, suggesting a nearly 4e ORR pathway even in the acid solution. IAG-C also shows a much better stability than the Pt/C electrode (decrease of only 5% for IAG-C while 32% for Pt/C over 15 000 s) and free from the methanol crossover-poisoning effects in the acid solution.

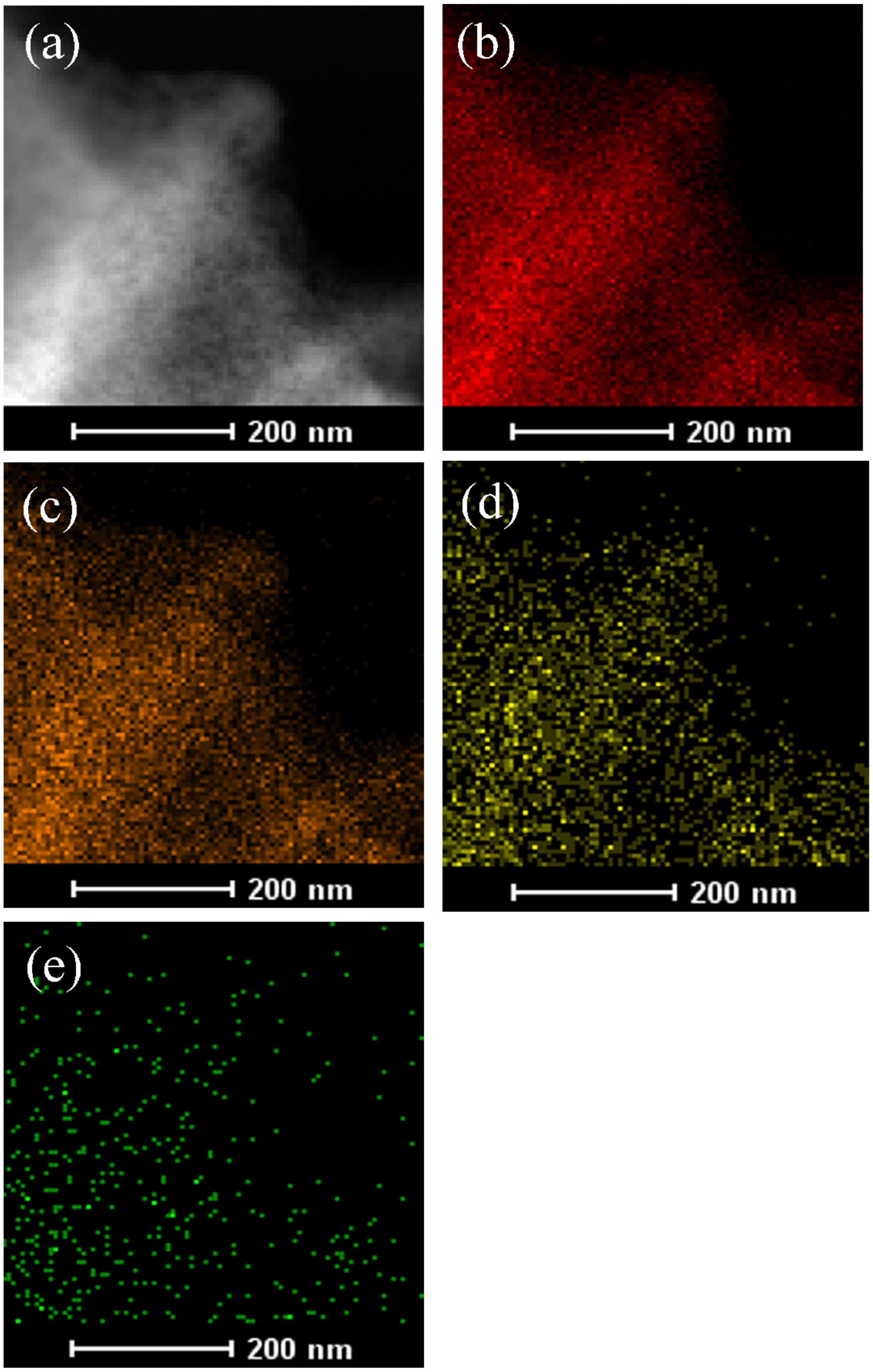

**Fig. S15.** (a) high-angle annular dark-field scanning transmission electron microscopy (STEM) image of the IAG-C catalyst; (b) C-, (c) N-, (d) O-, and (E) Fe-elemental mapping of the square region.

It is obvious that the intensity of N and Fe signals is much weaker than that of C due to the low content. Importantly, the iron and nitrogen signals are highly overlaid with each other, which is consistent with the previous reports that a metal species stabilized by nitrogen coordination are the active sites.

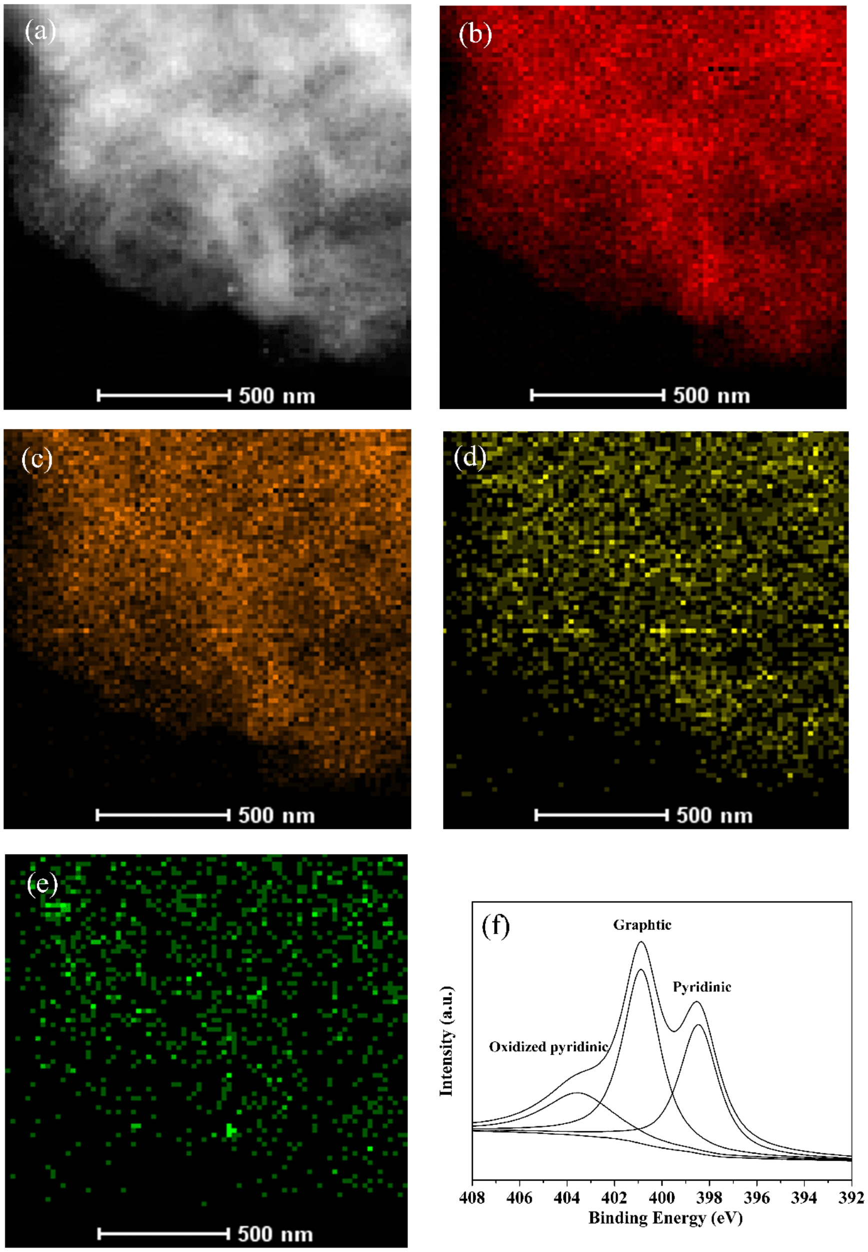

**Fig. S16.** (a) high-angle annular dark-field scanning transmission electron microscopy (STEM) image of the IAG-C catalyst; (b) C-, (c) N-, (d) O-, and (e) Fe-elemental mapping of the square region after stability test. (f) N 1s XPS spectra of IAG-C after stability test.

From the mapping analysis of Fig. S16, it can be found that the elements’ distribution is similar to the initial state (Fig. S15) after long-time test and the content of Fe remains almost unchanged, reflecting the stability of chemical structure in IAG-C catalyst. However, the long-term exposure to oxygen still leads to a certain decrease of the pyridinic N and increase of oxidized pyridinic N as shown in Fig. S16f. The performance loss during stability test appears to be directly related to the oxidation of pyridinic N and the formation of inactive oxide.

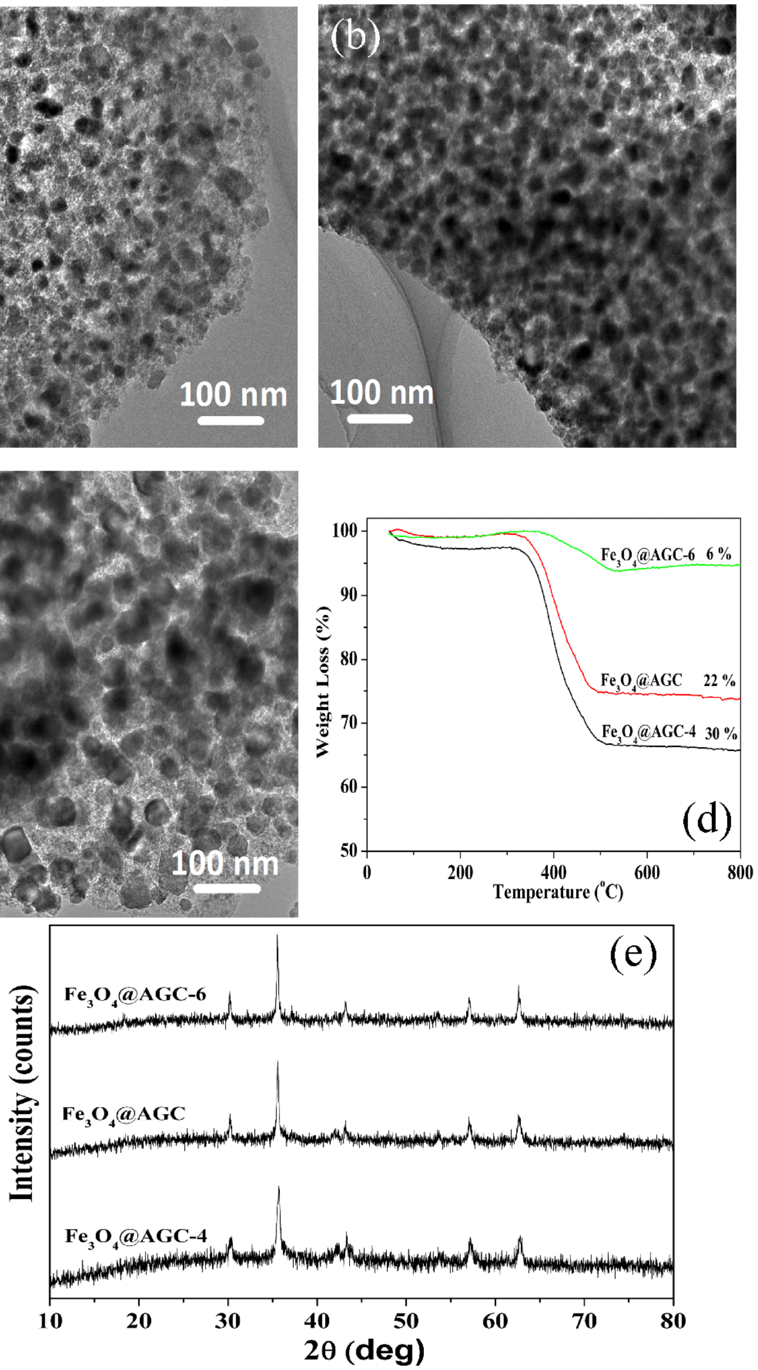

**Fig. S17.** TEM images of $Fe_3O_4$@AGC with different content of $Fe_3O_4$ in the hybrids: (a) $Fe_3O_4$@AGC-4, (b) $Fe_3O_4$@AGC, and (c) $Fe_3O_4$@AGC-6; (d) TG curves of the three hybrids to determine the content of carbon; (e) XRD patterns of three hybrids. The diffraction peaks of the composites are perfectly indexed to pure phase $Fe_3O_4$ (JCPDS No.65-3107).

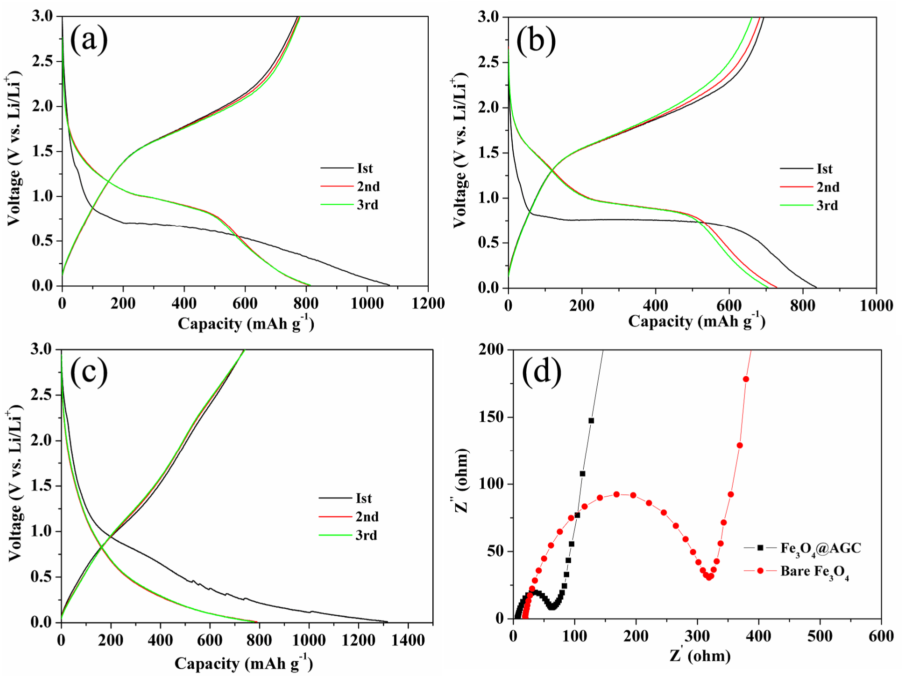

**Fig. S18** Charge-discharge curves of $Fe_3O_4$@AGC (a), bare $Fe_3O_4$ (b) and AGC (c) at the current density of 100 mA $g^{-1}$; (d) Nyquist plots for the $Fe_3O_4$@AGC and bare $Fe_3O_4$ based cells with lithium metal as counter electrode.

The capacities of three samples are 820, 700, and 770 mAh $g^{-1}$ for $Fe_3O_4$@AGC, bare $Fe_3O_4$, and AGC, respectively. According to the ratio of carbon, the contribution of carbon for capacity is 770×22% = 169.4. After subtracting the carbon's capacity, the real capacity of $Fe_3O_4$ in the hybrid $Fe_3O_4$@AGC is (820-169.4)/78% = 834.1, which is greatly improved compared to that of the bare $Fe_3O_4$ (700 mAh $g^{-1}$). The degree of increase is up to 19.2% and the results demonstrate as-prepared $Fe_3O_4$/N-doped carbon hybrid has advantages in lithium storage. AC impedance measurements are performed as shown in the Nyquist plots. It can be found that the diameter of the semicircle for $Fe_3O_4$@AGC electrodes in the high-medium frequency region is much smaller than that of bare $Fe_3O_4$, indicating lower contact and charge-transfer impedances of $Fe_3O_4$@AGC compared with bare $Fe_3O_4$.

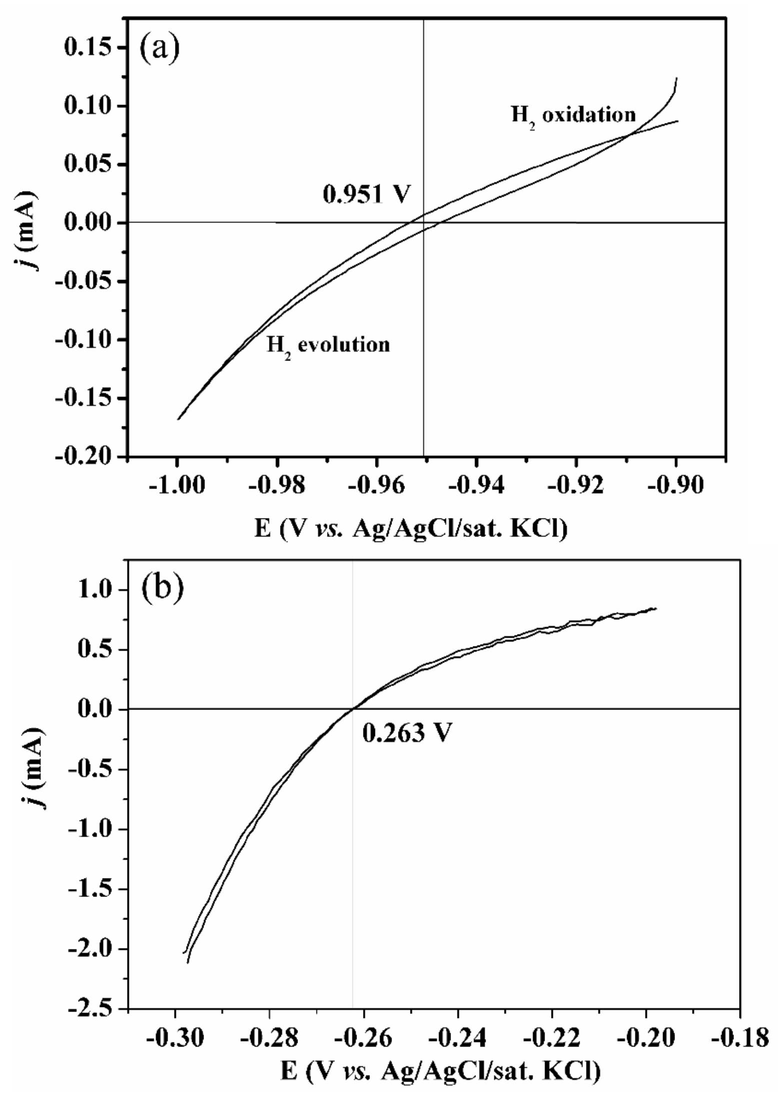

**Fig. S19**. The calibration CV curves of Ag/AgCl electrode (a) in 0.1 M KOH and (b) in 0.1 M $HClO_4$ with respect to RHE.